

# Full characterization of a focused wavefield with sub 100 nm resolution.

Robert Hoppe<sup>a</sup>, Vivienne Meier<sup>a</sup>, Jens Patommel<sup>a</sup>, Frank Seiboth<sup>a</sup>, Hae Ja Lee<sup>b</sup>, Bob Nagler<sup>b</sup>, Eric C. Galtier<sup>b</sup>, Brice Arnold<sup>b</sup>, Ulf Zastraub<sup>b</sup>, Jerome Hastings<sup>b</sup>, Daniel Nilsson<sup>c</sup>, Fredrik Uhlén<sup>c</sup>, Ulrich Vogt<sup>c</sup>, Hans M. Hertz<sup>c</sup>, Christian G. Schroer<sup>a</sup> and Andreas Schropp<sup>b</sup>

<sup>a</sup>Technische Universität Dresden, 01062 Dresden, Germany

<sup>b</sup>Linac Coherent Light Source, SLAC National Accelerator Laboratory, 2575 Sand Hill Road, Menlo Park, CA 94025, USA

<sup>c</sup>Biomedical & X-Ray Physics, KTH/Royal Institute of Technology, KTH-AlbaNova, SE-106 91, Stockholm, Sweden

## ABSTRACT

A hard x-ray free-electron laser (XFEL) provides an x-ray source with an extraordinary high peak-brilliance, a time structure with extremely short pulses and with a large degree of coherence, opening the door to new scientific fields. Many XFEL experiments require the x-ray beam to be focused to nanometer dimensions or, at least, benefit from such a focused beam. A detailed knowledge about the illuminating beam helps to interpret the measurements or is even inevitable to make full use of the focused beam. In this paper we report on focusing an XFEL beam to a transverse size of 125 nm and how we applied ptychographic imaging to measure the complex wavefield in the focal plane in terms of phase and amplitude. Propagating the wavefield back and forth we are able to reconstruct the full caustic of the beam, revealing aberrations of the nano-focusing optic. By this method we not only obtain the averaged illumination but also the wavefield of individual XFEL pulses.

**Keywords:** free-electron lasers, imaging and sensing, ptychography, xrays, compound refractive lenses

## 1. INTRODUCTION

Hard x-ray free-electron lasers (XFELs) differ from synchrotron radiation sources in the unique time structure of their radiation pulses. The ultra short highly intense pulses provide the possibility to perform new fascinating scientific experiments like the investigation of the dynamic behavior of atoms and molecules,<sup>1</sup> single shot imaging of biological structures,<sup>2,3</sup> coherent diffraction imaging of single molecules,<sup>4-6</sup> creating and observing matter in extreme conditions,<sup>7</sup> or monitor non-linear optical effects in the hard x-ray regime.<sup>8</sup>

Most of these experiments benefit from focusing the incoming XFEL beam onto the specimen, thereby increasing the fluence dramatically. A wide range of optics are available, that are able to cope with the high peak brilliance of an XFEL.<sup>9-11</sup> A detailed knowledge about the illuminating wavefield helps to evaluate the acquired data. Characterizing the focused beam of an XFEL is somehow different from doing so at a third generation synchrotron beam, thus knife-edge techniques are not applicable. A way out is to deploy imprint techniques: The beam destroys the illuminated region of a certain target, and the shape of the resulting crater is used to estimate the intensity distribution of the beam.<sup>10,12</sup>

An advanced method to measure the focused beam of an XFEL is to exert ptychographic imaging.<sup>13-17</sup> A test object is scanned by the beam while a far-field diffraction pattern is recorded at each scan point. An iterative phase retrieval algorithm<sup>18</sup> is applied to reconstruct phase and amplitude of the wavefield and the object, with high spatial resolution (see section 3). The knowledge of the wavefield in the object plane can be used, for example, to enhance the spatial resolution of imaging experiments by deconvolving the measured data with the shape of the illumination. Applying the Fresnel-Kirchhoff propagation formula,<sup>19</sup> the complex wavefield can be propagated along the optical axis, revealing the full caustic of the nanobeam.

In this paper we describe an experiment that we performed at the LCLS facility in May 2012.<sup>20</sup>

---

Further author information: (Send correspondence to Robert Hoppe.)

Robert Hoppe: E-mail: hoppe@xray-lens.de, Telephone: +49 351 463 38728

## 2. EXPERIMENTAL SETUP

The experiment was carried out at the matter in extreme condition (MEC) instrument located in the far experimental hall of the LCLS at SLAC, Stanford, USA, in a distance of 464 m behind the XFEL undulator. The electron energy was tuned to optimize the emittance of photons with an intended energy of 8200 eV. A 4 bounce Bartels monochromator decreased the relative energy bandwidth to below  $10^{-4}$ . As a trade-off, the combination of the unseeded SASE process and the monochromator led to a strong fluctuation of the photon flux by up to 3 to 4 orders of magnitude. A hard x-ray offset mirror (HOM) system redirected the beam to the experiment. The focusing lenses, the sample stages and the propagation path to the detector were situated within the experimental vacuum tank.

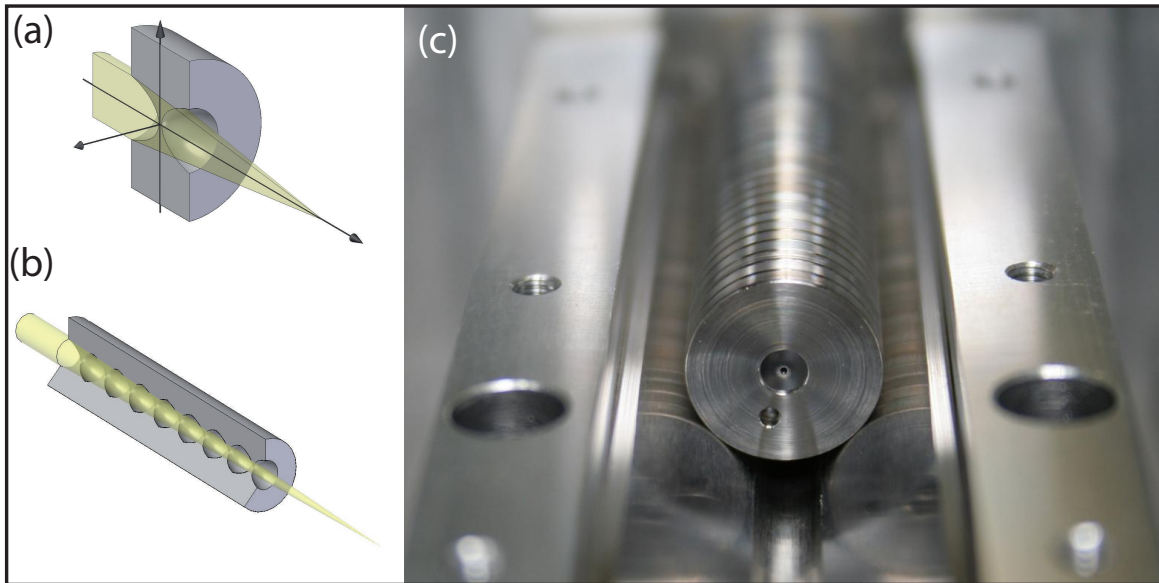


Figure 1. Parabolic compound refractive x-ray lens (CRL). a) Schematic drawing of a single lens. b) Schematic drawing of a stack of many single lenses. c) Photograph of a CRL holder, which holds an array of many single beryllium lenses.

The focusing was accomplished by a parabolic compound refractive x-ray lens (CRL).<sup>11,21,22</sup> A CRL consists of  $N$  single lenses made of beryllium stacked behind each other to reach the needed refraction strength, see figure 1. Each single lens is a beryllium disk into which the concave parabolic lens shape had been embossed from both sides, see Figure 1 a). The beryllium disks are framed by a metal ring such that the apex of the paraboloid is in the center of the ring with sub micrometer precision. To ensure that the apices of all single lenses are aligned in one single line, the metal frame of the single lenses are set into a high precision V-track. The entry and the exit apertures of the CRL are defined by a pair of pinholes that enclose the CRL. In the experiment we used a number of 20 single lenses with a radius  $R$  specified to  $50\ \mu\text{m}$  and a geometric aperture radius  $R_0$  of slightly more than  $150\ \mu\text{m}$ . The diffraction limited focus was expected to be generated at a distance 250 mm downstream the CRL with a full width at half maximum size of 115 nm and a gain in fluence of  $2 \times 10^6$  compared to the unfocused XFEL beam.

In the focused unattenuated XFEL beam the destruction limit of any material<sup>23</sup> is well exceeded. Ptychographic scanning of the sample in the full shot beam is therefore not feasible. Polished single crystal silicon absorbers were used to decrease the photon intensity, on the sample, below the sample damage threshold. The absorbers were also used to adapt the photon flux to the dynamic range of the detector.

The test object employed in the ptychography scan was a grid of  $40 \times 40$  similar Siemens stars etched into a  $1\ \mu\text{m}$  thick tungsten layer deposited onto a  $100\ \mu\text{m}$  thick CVD diamond substrate, see Figure 2(a). The period length of the grid was  $2\ \mu\text{m}$ , each Siemens star contained features with sizes in the range between 50 nm and 200 nm.

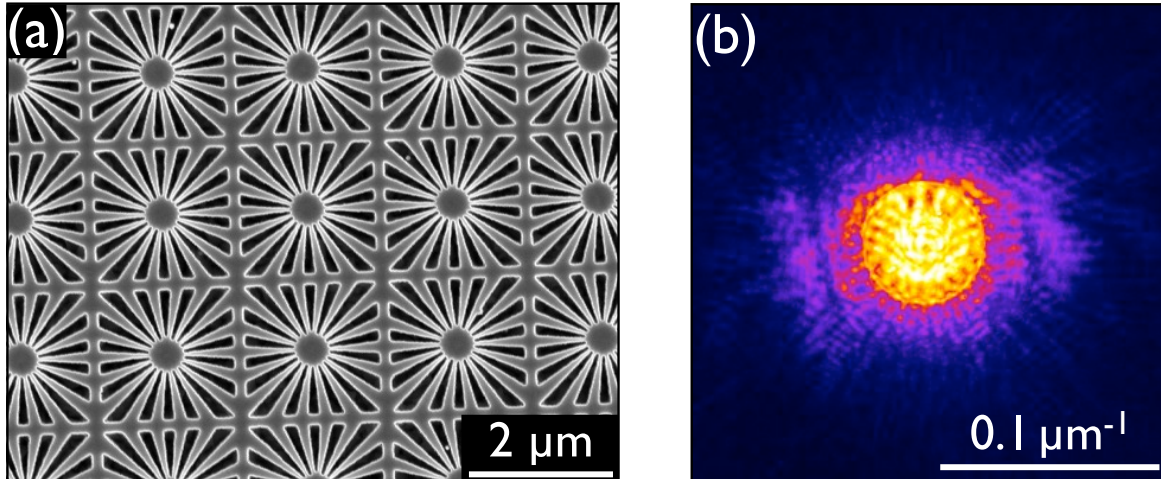


Figure 2. a) SEM image of the test object. b) Central region of a far-field diffraction pattern in logarithmic scale.

The sample was mounted on top of a scanner stage with nanometer resolution and an accuracy specified to below 10 nm. Far-field images were acquired by a cooled PIXIS CCD camera in a distance of 4.1 m behind the sample. Operated in  $4 \times 4$  binning mode, the detector recorded diffraction patterns that were sampled by  $512 \times 512$  pixels with an effective pixel size of  $54 \mu\text{m}$ , Figure 2(b).

### 3. PTYCHOGRAPHY

Coherent x-ray diffraction imaging (CXDI) is a well-established technique at FELs. Single shot images of identical samples are taken from different directions, combined and reconstructed to retrieve a spatial electron density map.<sup>1-3</sup> The method needs coherent light with highest intensities to measure photons scattered to the largest angles. Both requirements are fulfilled at FEL facilities. But CXDI is only applicable for samples that are smaller than the illuminating wavefield, so this method fails for extended objects. Another limitation of CXDI is that you need prior knowledge of the illumination, but this information is not available in most cases.

Ptychographic imaging techniques overcome these limitations by scanning an arbitrarily large region of the specimen with overlapping illumination between neighboring scan points while the far-field diffraction patterns are recorded at each scan point. Ptychography was originally developed to solve the phasing problem in electron microscopy structure analysis. Today, ptychographic imaging is an established method at third generation synchrotron radiation sources.<sup>24</sup> The diffraction patterns that are acquired in a ptychography scan allow the reconstruction of the object's complex-valued transmission function and of the complex wavefield in the object plane. The distinction of object function and illumination function is possible due to the overlap of adjacent illumination spots, which results in an overdetermined set of equations.

### 4. RESULTS

A  $2 \mu\text{m} \times 2 \mu\text{m}$  region of the sample was raster scanned by  $20 \times 20$  points with a step size of 100 nm in each direction, see Figure 3(a). The scan range was subdivided into four equal sets of  $5 \times 20$  raster points as indicated by the four colors in Figure 3. At each scan point 2 single-shot images were acquired to retrieve at least one properly illuminated pattern. This was necessary to take into account the strong photon flux variations between the single shots. The better of the two diffraction patterns was selected for reconstruction. But even the flux of the acquired images fluctuates by more than one order of magnitude. To ensure successful reconstruction, all images with a photon flux below a certain value (10% of the average) were rejected from being used in the reconstruction. Out of 800 acquired far-field images, only 381 were selected for reconstruction, see Figure 3(b). Emerging gaps in the scanned field of view do not affect the reconstruction quality, since the wide tails and the large transverse coherence length of the illumination ensure sufficient overlap between the scan points, even if

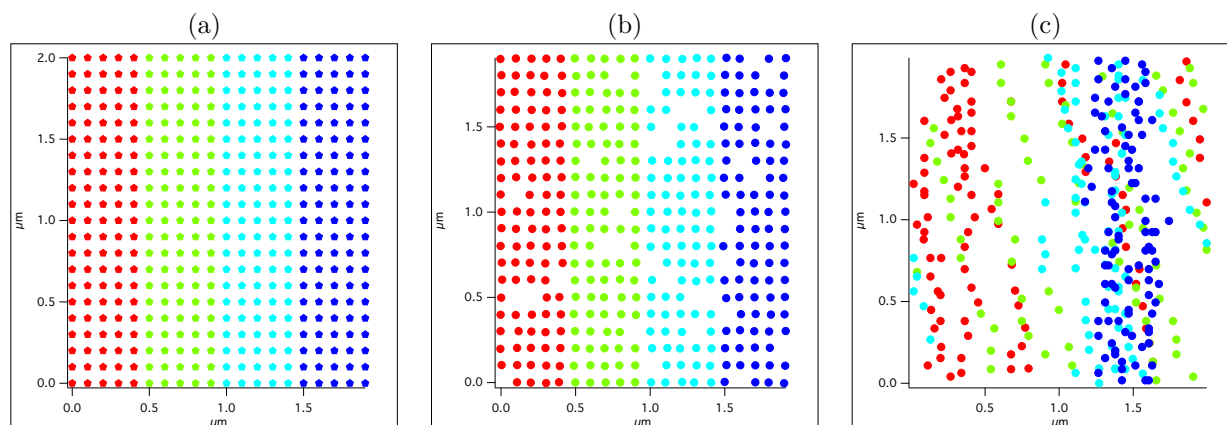


Figure 3. Raster scan points of the ptychographic scan. The scan was subdivided into four separated scans indicated by the four colors. (a) The designated raster points are located on a rectangular grid. Diffraction patterns with an integral photon dose below a certain threshold value were rejected. (b) shows the remaining scan points for which a proper diffraction pattern was recorded. (c) displays the positions of the scan points that were calculated by the reconstruction algorithm. The deviations from the intended positions are remarkable.

there are some voids. The remaining fluctuations of the flux are corrected by normalizing the diffraction patterns with respect to the measured photon flux of the XFEL pulses.

Ptychographic reconstruction turned out to be quite challenging, because the actual positions of the raster points differ significantly from the designated positions. Performing an initial reconstruction with the four subsets of diffraction patterns (indicated by the four colors in Figure 3) was only successful for each of the fourth subsets; reconstructions of the other three subsets do not converge to a reasonable solution. Figure 4(a) shows the phase shift induced by the object as a result of the reconstruction of the fourth subset. To reconstruct the algorithms used the raster point positions read from the scanning stage. As the expected raster point positions deviate considerably from the actual ones, the reconstruction suffers from artifacts and has a low resolution. To get rid of the artifacts and to enhance the spatial resolution, we developed a position refinement algorithm and applied it to the data.

Given a certain raster scan point, the refinement algorithm simulates the diffraction pattern and calculates the least square distance between the simulated and the measured diffraction pattern as a function of the position. The refined position of the recent scan point minimizes the least square distance. Iterating over all scan points, the algorithm finds a set of refined positions that can be used as input for a further ptychographic reconstruction. Figure 4(b) depicts the reconstructed phase of the object transmission function after ptychographic reconstruction with refined positions, in which, again, only the fourth subset of diffraction patterns was used.

In a next step, the reconstructed object and illumination obtained so far can be utilized to apply ptychographic reconstruction all the subsets of diffraction patterns. Alternating position refinement and ptychographic reconstruction with differing update rules leads to the final reconstruction shown in Figure 4(c). A comparison between the designated positions shown in 3(a) and the final refined positions illustrated in Figure 3(c) reveals strong deviations. Obviously, due to thermal drifts and instabilities of the setup.

To be able to compare the resolution of different imaging techniques, we define the spatial resolution as the FWHM of the deviation of the edge-transfer function determined from a line profile over a certain feature in the image, at which the feature should be a kind of sharp edge. Applying this to Figure 4(c) one finds a spatial resolution of 70 nm.

The algorithm that we used for ptychographic reconstruction assumes a constant illumination for each scan point and neglects variations of the illumination between different exposures. At third generation synchrotron radiation sources the shape of the illumination does not change very much, the monotonically decreasing photon flux – if present at all – is corrected by normalizing the diffraction patterns with respect to the measured photon flux. It was not clear in advance, if the same is true in case of an XFEL source. If the shape of the illumination

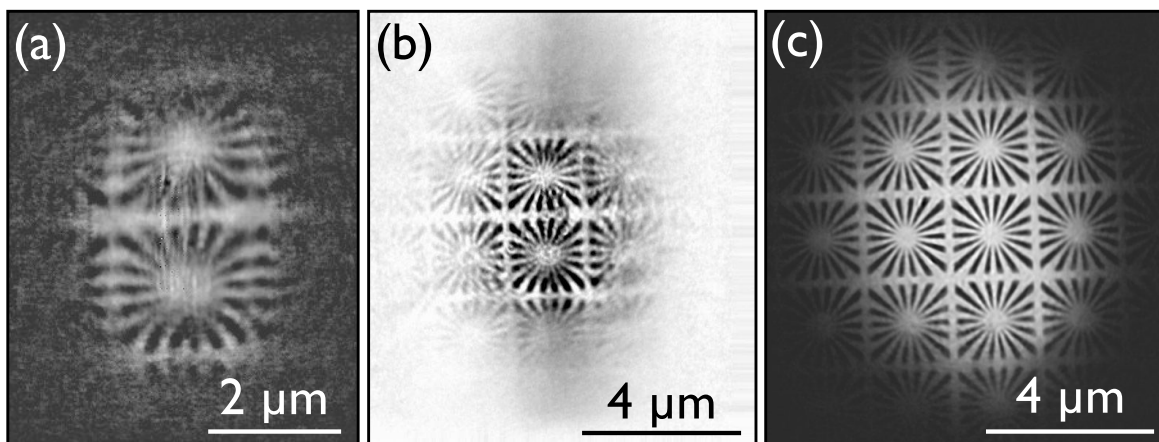


Figure 4. Reconstructed phase shift induced by the test object. Zero phase shift is represented by black. (a) Object phase after the initial reconstruction of the fourth subset of diffraction patterns. The algorithm use the designated scan point positions. (b) Object phase after the first iteration of the position refinement algorithm, applied to the fourth subset of diffraction patterns. The calculated positions were used as initial values to reconstruct the whole scan including all four subsets. After 6 iterations of ptychographic reconstruction and position refinement we obtain the object phase as shown in (c).

changes too much from single shot to single shot, ptychographic reconstruction fails. As shown in Figure 4, ptychography was able to reconstruct the object correctly, compare figure 2 a. The geometric shape of the reconstruction matches that of the original object in very good agreement. In addition, the reconstructed phase shift value of  $-1.8$  rad conforms to the value of  $-1.9$  rad, which is theoretically expected for a  $1 \mu\text{m}$  thick tungsten layer at  $8.2 \text{ keV}$ .

There are further possibilities to check for consistency. For example, the reconstructed wavefield can be numerically propagated to the detector plane, where its intensity distribution can be compared with the measured intensity of the focused beam without sample. We found that the reconstructed far-field intensity distribution represents all the features in very good agreement with the measured intensity.<sup>20</sup>

Nevertheless, the reconstructed wavefield is only an average over the single shot wavefields. It is possible to use the ptychography data to reconstruct the wavefield for each individual scan point. For this we use the reconstructed object function and the refined scan point positions to execute another ptychographic reconstruction. But now the object function is kept fixed and the individual wavefield retrieved at each scan point is stored separately instead of being used to update the global (averaged) illumination. Figure 5 illustrates the averaged illumination function (b) in comparison with the individual wavefields of two scan points (a) and (c), respectively. There is almost no difference in the shape of the wavefields. The larger noise level of an individual wavefield is caused by a much lower signal, since the individual wavefield is retrieved from only one diffraction pattern, while the averaged wavefield is determined by several hundreds of diffraction patterns. The shape of a focused XFEL beam remains nearly the same from pulse to pulse, although the illumination function on the aperture of the lens .

One important advantage of knowing both, real and imaginary part of the illumination function (or phase and amplitude, respectively) is the possibility to propagate the wavefield back and forth applying the Fresnel-Kirchhoff propagation formula.<sup>19</sup> This allows to reconstruct the full three-dimensional caustic. Figure 6 illustrates the three-dimensional complex caustic in the range  $\pm 20 \text{ mm}$  around the focal plane; the complex values are represented by amplitude (hue-coded) and by phase (color-coded). An aberration-free CRL is expected to generate a Gaussian beam with a waist in the focal plane. The reconstructed caustic, however, shows spherical aberrations: rays that pass the lens near the optical axis are refracted with a shorter focal distance than rays that pass the lens further away from the optical axis. From this fact we conclude that the shape of the refractive lenses is not a perfect paraboloid. The apex of the paraboloid does not coincide with the axis of rotation (optical axis). The parabolic shape is slightly shifted in a way to increased curvature near the optical axis, while the curvature away

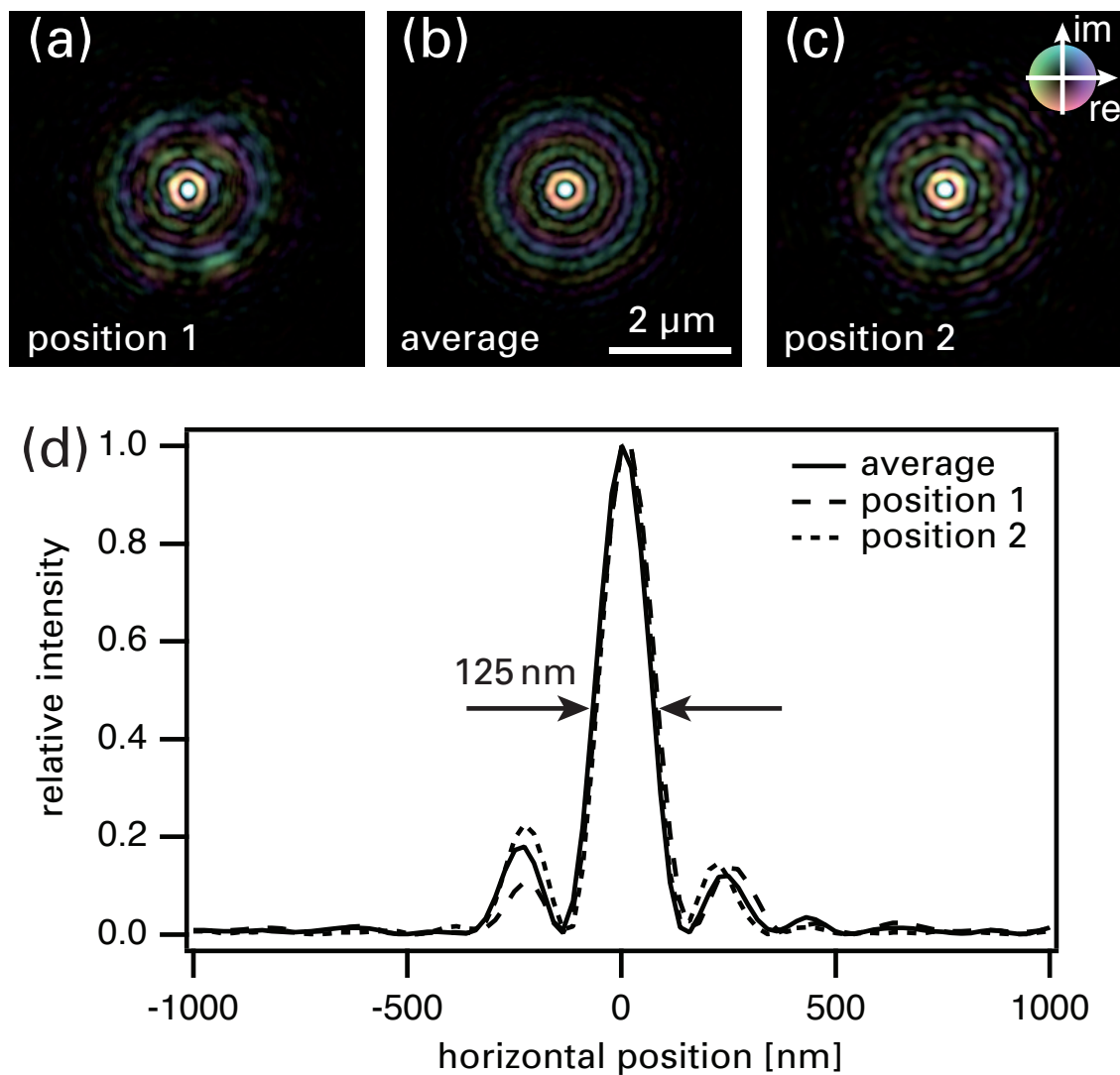


Figure 5. Reconstructed illuminating wavefield. (b) shows the illumination averaged over all 381 single shots. (a) and (c) show reconstructions of two individual shots. (d) The line profile through the focus reveals a focus size of 125 nm FWHM. Variations in the intensity distribution are present but only in the lower intensity species. The central focal spot is almost the same for each single shot.

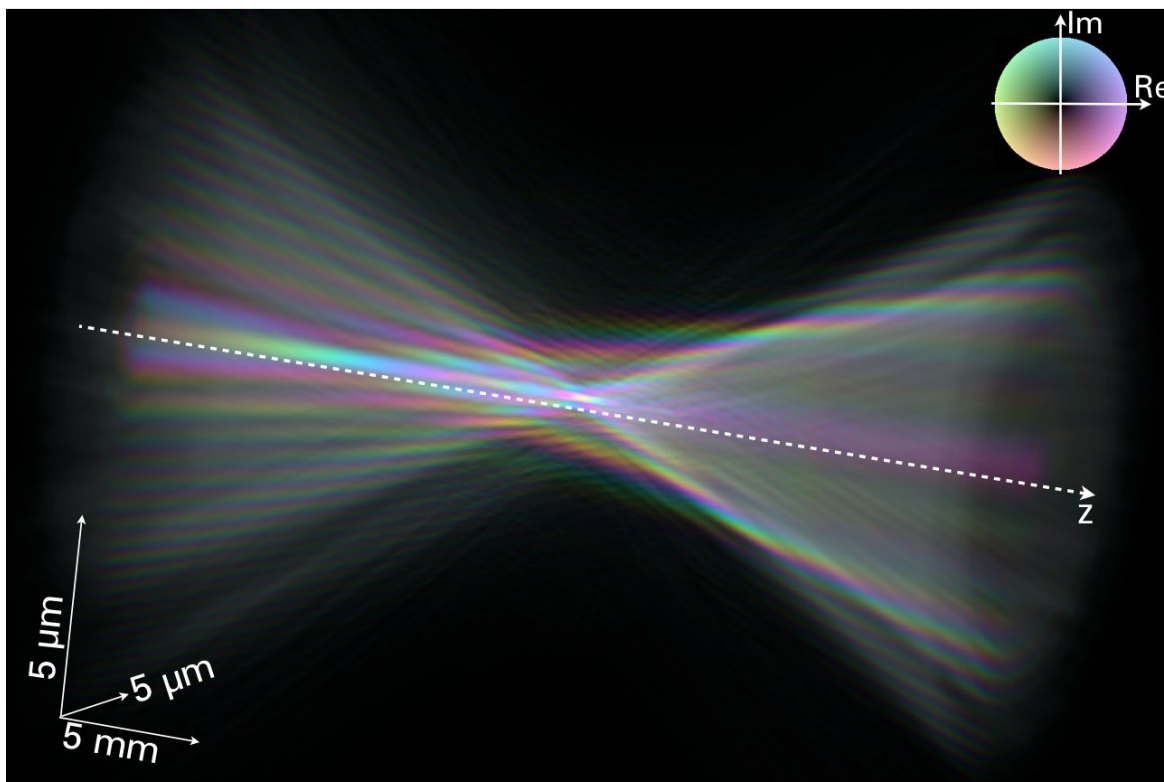


Figure 6. Three-dimensional illustration of the complex illumination field along the optical axis. The reconstructed illuminating wavefield can be propagated along the optical axis. The resulting intensities are coded by the luminosity of a voxel and the phase of the wavefield is represented by color. Spherical aberrations of the CRLs are clearly visible. For the rays passing close to the optical axis the focal length is shorter than for these passing the optic at its periphery.

from the center line is weaker. This information serves as input to the improved fabrications of beryllium CRLs by RX-Optics ([www.rxoptics.de](http://www.rxoptics.de)).

## 5. SUMMARY

We have shown that parabolic compound refractive x-ray lenses (CRLs) made of beryllium are well-suited to focus the hard x rays of an FEL beam to a spot size of about 125 nm FWHM. The shape of the intensity distribution are observed to be very stable from pulse to pulse, even though the flux varied by more than three orders of magnitude. This variation results from fluctuation of the x-ray energy from pulse to pulse. We proved that ptychography is a proper technique to analyze an attenuated focused XFEL beam, providing information about amplitude and phase with a resolution better than 70 nm. Moreover, the method can be expanded to analyze unattenuated XFEL pulses, employing periodic test structures. For each scan point another different but similar test structure would be illuminated, allowing each test structure to be destroyed by the individual pulse. The reconstructed complex wavefield can be propagated along the optical axis to obtain the full three-dimensional caustic. This allows to analyze distortions of the ideal caustic and to identify aberrations of the focusing optic. The knowledge of the intensity distribution of the XFEL beam near the focal plane will be useful to evaluate and understand the measured data in many experiments that make use of a focused beam.

## REFERENCES

1. H. N. Chapman, P. Fromme, A. Barty, T. A. White, R. A. Kirian, A. Aquila, M. S. Hunter, J. Schulz, D. P. DePonte, U. Weierstall, R. B. Doak, F. R. N. C. Maia, A. V. Martin, I. Schlichting, L. Lomb, N. Coppola, R. L. Shoeman, S. W. Epp, R. Hartmann, D. Rolles, A. Rudenko, L. Foucar, N. Kimmel, G. Weidenspointner,

- P. Holl, M. Liang, M. Barthelmess, C. Caleman, S. Boutet, M. J. Bogan, J. Krzywinski, C. Bostedt, S. Bajt, L. Gumprecht, B. Rudek, B. Erk, C. Schmidt, A. Hömke, C. Reich, D. Pietschner, L. Strüder, G. Hauser, H. Gorke, J. Ullrich, S. Herrmann, G. Schaller, F. Schopper, H. Soltau, K.-U. Kühnel, M. Messerschmidt, J. D. Bozek, S. P. Hau-Riege, M. Frank, C. Y. Hampton, R. G. Sierra, D. Starodub, G. J. Williams, J. Hajdu, N. Timneanu, M. M. Seibert, J. Andreasson, A. Rucker, O. Jönsson, M. Svenda, S. Stern, K. Nass, R. Andritschke, C.-D. Schröter, F. Krasniqi, M. Bott, K. E. Schmidt, X. Wang, I. Grotjohann, J. M. Holton, T. R. M. Barends, R. Neutze, S. Marchesini, R. Fromme, S. Schorb, D. Rupp, M. Adolph, T. Gorkhover, I. Andersson, H. Hirsemann, G. Potdevin, H. Graafsma, B. Nilsson, and J. C. H. Spence, "Femtosecond x-ray protein nanocrystallography," *Nature* **470**(7332), pp. 73–77, 2011.
2. R. Koopmann, K. Cupelli, L. Redecke, K. Nass, D. P. DePonte, T. A. White, F. Stellato, D. Rehders, M. Liang, J. Andreasson, A. Aquila, S. Bajt, M. Barthelmess, A. Barty, M. J. Bogan, C. Bostedt, S. Boutet, J. D. Bozek, C. Caleman, N. Coppola, J. Davidsson, R. B. Doak, T. Ekeberg, S. W. Epp, B. Erk, H. Fleckenstein, L. Foucar, H. Graafsma, L. Gumprecht, J. Hajdu, C. Y. Hampton, A. Hartmann, R. Hartmann, G. Hauser, H. Hirsemann, P. Holl, M. S. Hunter, S. Kassemeyer, R. A. Kirian, L. Lomb, F. R. N. C. Maia, N. Kimmel, A. V. Martin, M. Messerschmidt, C. Reich, D. Rolles, B. Rudek, A. Rudenko, I. Schlichting, J. Schulz, M. M. Seibert, R. L. Shoeman, R. G. Sierra, H. Soltau, S. Stern, L. Strüder, N. Timneanu, J. Ullrich, X. Wang, G. Weidenspointner, U. Weierstall, G. J. Williams, C. B. Wunderer, P. Fromme, J. C. H. Spence, T. Stehle, H. N. Chapman, C. Betzel, and M. Duszynko, "In vivo protein crystallization opens new routes in structural biology," *Nature Methods* **9**(3), pp. 259–262, 2012.
  3. L. C. Johansson, D. Arnlund, T. A. White, G. Katona, D. P. DePonte, U. Weierstall, R. B. Doak, R. L. Shoeman, L. Lomb, E. Malmerberg, J. Davidsson, K. Nass, M. Liang, J. Andreasson, A. Aquila, S. Bajt, M. Barthelmess, A. Barty, M. J. Bogan, C. Bostedt, J. D. Bozek, C. Caleman, R. Coffee, N. Coppola, T. Ekeberg, S. W. Epp, B. Erk, H. Fleckenstein, L. Foucar, H. Graafsma, L. Gumprecht, J. Hajdu, C. Y. Hampton, R. Hartmann, A. Hartmann, G. Hauser, H. Hirsemann, P. Holl, M. S. Hunter, S. Kassemeyer, N. Kimmel, R. A. Kirian, F. R. N. C. Maia, S. Marchesini, A. V. Martin, C. Reich, D. Rolles, B. Rudek, A. Rudenko, I. Schlichting, J. Schulz, M. M. Seibert, R. G. Sierra, H. Soltau, D. Starodub, F. Stellato, S. Stern, L. Strüder, N. Timneanu, J. Ullrich, W. Y. Wahlgren, X. Wang, G. Weidenspointner, C. Wunderer, P. Fromme, H. N. Chapman, J. C. H. Spence, and R. Neutze, "Lipidic phase membrane protein serial femtosecond crystallography," *Nat Meth* **9**, pp. 263–265, 03 2012.
  4. R. Neutze, R. Wouts, D. van der Spoel, E. Weckert, and J. Hajdu, "Potential for biomolecular imaging with femtosecond x-ray pulses," *Nature* **406**(6797), pp. 752–757, 2000.
  5. K. J. Gaffney and H. N. Chapman, "Imaging atomic structure and dynamics with ultrafast x-ray scattering," *Science* **316**(5830), pp. 1444–1448, 2007.
  6. B. Ziaja, H. N. Chapman, R. Fäustlin, S. Hau-Riege, Z. Jurek, A. V. Martin, S. Toleikis, F. Wang, E. Weckert, and R. Santra, "Limitations of coherent diffractive imaging of single objects due to their damage by intense x-ray radiation," *New Journal of Physics* **14**(11), p. 115015, 2012.
  7. S. M. Vinko, O. Ciricosta, B. I. Cho, K. Engelhorn, H. K. Chung, C. R. D. Brown, T. Burian, J. Chalupsky, R. W. Falcone, C. Graves, V. Hajkova, A. Higginbotham, L. Juha, J. Krzywinski, H. J. Lee, M. Messerschmidt, C. D. Murphy, Y. Ping, A. Scherz, W. Schlotter, S. Toleikis, J. J. Turner, L. Vysin, T. Wang, B. Wu, U. Zastra, D. Zhu, R. W. Lee, P. A. Heimann, B. Nagler, and J. S. Wark, "Creation and diagnosis of a solid-density plasma with an x-ray free-electron laser," *Nature* **482**, pp. 59–62, 02 2012.
  8. T. E. Glover, D. M. Fritz, M. Cammarata, T. K. Allison, S. Coh, J. M. Feldkamp, H. Lemke, D. Zhu, Y. Feng, R. N. Coffee, M. Fuchs, S. Ghimire, J. Chen, S. Shwartz, D. A. Reis, S. E. Harris, and J. B. Hastings, "X-ray and optical wave mixing," *Nature* **488**, pp. 603–608, 08 2012.
  9. H. Mimura, S. Morita, T. Kimura, D. Yamakawa, W. Lin, Y. Uehara, S. Matsuyama, H. Yumoto, H. Ohashi, K. Tamasaku, Y. Nishino, M. Yabashi, T. Ishikawa, H. Ohmori, and K. Yamauchi, "Focusing mirror for x-ray free-electron lasers," *Review of Scientific Instruments* **79**(8), p. 083104, 2008.
  10. C. David, S. Gorelick, S. Rutishauser, J. Krzywinski, J. Vila-Comamala, V. A. Guzenko, O. Bunk, E. Färm, M. Ritala, and M. Cammarata, "Nanofocusing of hard X-ray free electron laser pulses using diamond based Fresnel zone plates," *Scientific Reports* **1**, 2011.

11. C. G. Schroer, B. Benner, M. Kuhlmann, O. Kurapova, B. Lengeler, F. Zontone, A. Snigirev, I. Snigireva, and H. Schulte-Schrepping, "Focusing hard x-ray FEL beams with parabolic refractive lenses," in *Fourth Generation X-Ray Sources and Optics II*, S. G. Biedron, W. Eberhardt, T. Ishikawa, and R. O. Tatchyn, eds., *Proceedings of the SPIE* **5534**, pp. 116–124, 2004.
12. J. Chalupský, J. Krzywinski, L. Juha, V. Hájková, J. Cihelka, T. Burian, L. Vysín, J. Gaudin, A. Gleeson, M. Jurek, A. R. Khorsand, D. Klinger, H. Wabnitz, R. Sobierajski, M. Störmer, K. Tiedtke, and S. Toleikis, "Spot size characterization of focused non-gaussian x-ray laser beams," *Optics Express* **18**, pp. 27836–27845, 2010.
13. A. Schropp, P. Boye, J. M. Feldkamp, R. Hoppe, J. Patommel, D. Samberg, S. Stephan, K. Giewekemeyer, R. N. Wilke, T. Salditt, J. Gulden, A. P. Mancuso, I. A. Vartanyants, E. Weckert, S. Schöder, M. Burghammer, and C. G. Schroer, "Hard x-ray nanobeam characterization by coherent diffraction microscopy," *Appl. Phys. Lett.* **96**(9), p. 091102, 2010.
14. C. M. Kewish, M. Guizar-Sicairos, C. Liu, J. Qian, B. Shi, C. Benson, A. M. Khounsary, J. Vila-Comamala, O. Bunk, J. R. Fienup, A. T. Macrander, and L. Assoufid, "Reconstruction of an astigmatic hard x-ray beam and alignment of k-b mirrors from ptychographic coherent diffraction data," *Opt. Express* **18**, pp. 23420–23427, Oct 2010.
15. C. M. Kewish, P. Thibault, M. Dierolf, O. Bunk, A. Menzel, J. Vila-Comamala, K. Jefimovs, and F. Pfeiffer, "Ptychographic characterization of the wavefield in the focus of reflective hard x-ray optics," *Ultramicroscopy* **110**(4), pp. 325 – 329, 2010.
16. J. Vila-Comamala, A. Diaz, M. Guizar-Sicairos, A. Manton, C. M. Kewish, A. Menzel, O. Bunk, and C. David, "Characterization of high-resolution diffractive x-ray optics by ptychographic coherent diffractive imaging," *Opt. Express* **19**, pp. 21333–21344, Oct 2011.
17. S. Hönig, R. Hoppe, J. Patommel, A. Schropp, S. Stephan, S. Schöder, M. Burghammer, and C. G. Schroer, "Full optical characterization of coherent x-ray nanobeams by ptychographic imaging," *Optics Express* **19**(17), pp. 16324–16329, 2011.
18. A. M. Maiden and J. M. Rodenburg, "An improved ptychographical phase retrieval algorithm for diffractive imaging," *Ultramicroscopy* **109**(10), pp. 1256–1262, 2009.
19. M. Born, E. Wolf, A. B. Bhatia, P. C. Clemmow, D. Gabor, A. R. Stokes, A. M. Taylor, P. A. Wayman, and W. L. Wilcock, *Principles of Optics: Electromagnetic Theory of Propagation, Interference and Diffraction of Light*, Cambridge University Press, 7th ed., October 1999.
20. A. Schropp, R. Hoppe, V. Meier, J. Patommel, F. Seiboth, H. J. Lee, B. Nagler, E. C. Galtier, B. Arnold, U. Zastrau, J. B. Hastings, D. Nilsson, F. Uhlen, U. Vogt, H. M. Hertz, and C. G. Schroer, "Full spatial characterization of a nanofocused x-ray free-electron laser beam by ptychographic imaging," *Sci. Rep.* **3**, 04 2013.
21. B. Lengeler, C. Schroer, J. Tümmler, B. Benner, M. Richwin, A. Snigirev, I. Snigireva, and M. Drakopoulos, "Imaging by parabolic refractive lenses in the hard x-ray range," *J. Synchrotron Rad.* **6**, pp. 1153–1167, 1999.
22. B. Lengeler, C. G. Schroer, M. Kuhlmann, B. Benner, T. F. Günzler, O. Kurapova, F. Zontone, A. Snigirev, and I. Snigireva, "Refractive x-ray lenses," *J. Phys. D: Appl. Phys.* **38**, pp. A218–A222, 2005.
23. G. Doumy, C. Roedig, S.-K. Son, C. I. Blaga, A. D. DiChiara, R. Santra, N. Berrah, C. Bostedt, J. D. Bozek, P. H. Bucksbaum, J. P. Cryan, L. Fang, S. Ghimire, J. M. Glowina, M. Hoener, E. P. Kanter, B. Krässig, M. Kuebel, M. Messerschmidt, G. G. Paulus, D. A. Reis, N. Rohringer, L. Young, P. Agostini, and L. F. DiMauro, "Nonlinear atomic response to intense ultrashort x rays," *Phys. Rev. Lett.* **106**, p. 083002, Feb 2011.
24. J. M. Rodenburg and H. M. L. Faulkner, "A phase retrieval algorithm for shifting illumination," *Appl. Phys. Lett.* **85**(20), pp. 4795–4797, 2004.